sustainability

MDPI

Article

Synergistic and Trade-Off Influences of Combined $PM_{2.5}$-O_3 Pollution in the Shenyang Metropolitan Area, China: A Comparative Land Use Regression Analysis

Tuo Shi *, Xuemei Yuan, Chunjiao Li and Fangyuan Li

College of Life Science, Shenyang Normal University, Shenyang 110034, China; 13158506785@163.com (X.Y.); lichunjiao@synu.edu.cn (C.L.); lfy010902@163.com (F.L.)
* Correspondence: shi_tuo@synu.edu.cn

Abstract

Fine particulate matter ($PM_{2.5}$) and ozone (O_3) are the main pollutants affecting the air quality in China, yet their common influencing factors and spatial patterns remain unclear. Focusing on the year 2020, this study adopted the least absolute shrinkage and selection operator algorithm to construct land use regression models with 34 environmental variables for the O_3 concentration at the air quality monitoring stations in the Shenyang Metropolitan Area. For comparison, $PM_{2.5}$ models had been developed in our previous work using the same approach. Model performance was satisfactory (cross-validated R^2 = 0.49–0.81 for O_3; 0.56–0.65 for $PM_{2.5}$ in our previous study), confirming the robustness of the approach. The results showed that: (1) Tree cover and grassland exerted synergistic, co-directional mitigation on both pollutants, whereas built-up areas and permanent water bodies were positively associated with their concentrations; (2) Longitude, elevation, and population, as well as atmospheric components such as nitrous dioxide column density and aerosol optical depth, displayed opposite effects on both pollutants, indicating trade-offs; (3) Spatially, $PM_{2.5}$ played the dominant role in shaping the pattern of combined pollution, with higher $PM_{2.5}$ levels than O_3 in nearly half of the area (46.97%), while O_3-dominant regions were rare (4.27%) and mostly confined to localized zones. This study contributes to a deeper understanding of the synergies and trade-offs driving $PM_{2.5}$ and O_3 pollution as well as providing a scientific basis for formulating policies on integrated control measures against combined pollution.

Keywords: O_3; $PM_{2.5}$; combined pollution; land use regression; synergy and trade-off

check for updates

Academic Editor: Elena Cristina Rada

Received: 17 July 2025
Revised: 25 August 2025
Accepted: 3 September 2025
Published: 6 September 2025

Citation: Shi, T.; Yuan, X.; Li, C.; Li, F. Synergistic and Trade-Off Influences of Combined $PM_{2.5}$-O_3 Pollution in the Shenyang Metropolitan Area, China: A Comparative Land Use Regression Analysis. *Sustainability* **2025**, *17*, 8046. https://doi.org/10.3390/su17178046

Copyright: © 2025 by the authors. Licensee MDPI, Basel, Switzerland. This article is an open access article distributed under the terms and conditions of the Creative Commons Attribution (CC BY) license (https://creativecommons.org/licenses/by/4.0/).

1. Introduction

The air pollution problem in China has changed from an accumulative problem of a single pollutant to a complex situation caused by the coexistence and interaction of multiple pollutants [1]. In 2023, 31% and 23.3% of the 339 cities at the prefecture level or higher, including sub-provincial and centrally administered municipalities in China, exceeded the standards for fine particulate matter ($PM_{2.5}$) and ozone (O_3) concentrations, respectively. On average, these cities experienced about 53 days of exceedances, during which $PM_{2.5}$ and O_3 were the primary pollutants responsible, accounting for 35.5% and 40.1% of the total exceedance days, respectively [2]. Globally, a total of 8.34 million deaths were estimated to be attributable to $PM_{2.5}$ and O_3 pollution, with the majority of the death burden related to cardiovascular and metabolic disease [3]. $PM_{2.5}$ can absorb microorganisms or

harmful components and directly enter the alveoli through the respiratory tract, causing diseases [4,5]. In addition, exposure to $PM_{2.5}$ may induce alveolar inflammation, which can facilitate the entry of certain viruses (e.g., COVID-19) [6]. Furthermore, the increase in $PM_{2.5}$ concentration in the atmosphere can exacerbate haze and influence phenomena such as cloud cover, monsoon strength, and the radiation balance of the surface-atmosphere system [7]. As a strong oxidant in the troposphere, high concentrations of near-surface O_3 can also have adverse effects on human health, plant growth, and ecosystem productivity [8].

$PM_{2.5}$ comes from various sources, including directly from industrial emissions, vehicle exhaust, and coal burning, as well as secondary formation through atmospheric chemical reactions of gaseous precursors such as sulfur dioxide and nitrogen oxides (NO_x) [9,10]. These transformations involve complex processes such as gas–particle conversion and photochemical oxidation. The formation of O_3 mainly depends on photochemical reactions in the atmosphere. Under the sun's ultraviolet rays, volatile organic compounds (VOCs) and NO_x generate O_3 through a chain reaction, while certain $PM_{2.5}$ constituents, including black carbon and metal oxides, may catalyze and enhance this process [11,12]. Meanwhile, O_3 can react with VOCs to form secondary organic aerosols, thereby increasing the concentration of $PM_{2.5}$. In addition to these internal coupling mechanisms, the relationship between $PM_{2.5}$ and O_3 is affected by meteorological conditions, emissions, land use, and spatial patterns [13–16]. Under different conditions, the relationship can be entirely the opposite. For example, Shao et al. found that there was a significant positive correlation between the peak concentrations of $PM_{2.5}$ and O_3 in Nanjing during summer, and the characteristics of compound air pollution were quite obvious [17]. However, Wang et al. found a significant negative correlation between $PM_{2.5}$ and O_3 concentration in Shenyang [18]. The complex chemical coupling and numerous influencing factors make the joint control of these two pollutants challenging.

In the field of ecosystem service research, the "trade-off/synergistic" relationship is often used to measure the mutual offset or mutual gain between different ecosystem services. There may also be trade-offs and synergies in the combined pollution of $PM_{2.5}$ and O_3 that affect their levels. It is essential to clarify the role of the influencing factors between the two pollutants for effective joint control, but there is still insufficient relevant research on this topic.

A land use regression (LUR) model is a stochastic model that can predict pollutant concentrations at unknown points by constructing statistical relationships between pollutant concentrations and environmental variables at monitoring points or sampling sites. LUR models can be applied at many spatial scales and are widely used in studying environmental exposure and pollution patterns [19,20]. A variety of algorithms can be used to fit LUR models. Ma and Shi et al. compared the applicability and limitations of fitting algorithms when constructing LUR models [20,21]. The least absolute shrinkage and selection operator (LASSO) is a machine learning method based on linear regression that excels at enhancing model interpretability by promoting sparsity through the penalization of coefficient magnitudes; it selects only the most influential variables, and it is effective when dealing with multi-dimensional data and potential multicollinearity [22]. The LASSO algorithm has been applied to fit LUR models in numerous studies [14,21,23].

Urban agglomerations/metropolitan regions, which are characterized by high population density and intense human activities, exhibit diversified land uses and spatial patterns owing to concentrated socioeconomic interactions. Shenyang Metropolitan Area (SYMA), officially designated in 2023 as China's ninth national-level metropolitan area and the first in Northeast China, is a major heavy industrial cluster with a distinctive economic and geographic profile. Its dense population, high energy consumption, and industrial structure impose severe pressures on air quality, making it a representative case for studying combined $PM_{2.5}$–O_3 pollution [21]. In previous studies, we used the LASSO algorithm to predict the main factors

affecting changes in $PM_{2.5}$ concentration and pollution patterns in SYMA and found that LUR models explained 62–70% of $PM_{2.5}$ variability, with a positive correlation with surface pressure and a negative correlation with elevation and tree cover. Landscape aggregation at 2000 m was negatively associated with $PM_{2.5}$ concentrations, while fragmentation at 5000 m also showed a negative correlation with concentrations. Shrubland (spring) and bare areas (autumn) increased concentrations, contrasting with consistent mitigation by tree cover in winter. Vegetation structure proved vital for $PM_{2.5}$ reduction, highlighting the importance of multiscale landscape strategies for sustainable pollution control. As another major pollutant in this region, O_3 has a complex interaction mechanism with $PM_{2.5}$, but its exact role in SYMA remains unclear. Building on the analytical framework of Wu et al. (2021) in the Pearl River Delta (PRD) [14], this study extends the analysis to the SYMA in Northeast China, which differs substantially in geographical location, climatic conditions, and industrial structure. Our study explores the factors driving trade-off or synergistic effects on $PM_{2.5}$ and O_3 pollution, providing a comparative perspective that broadens the spatial coverage of such research. For this purpose, we built O_3 LUR models to answer the following questions: (1) What factors play major roles in O_3 spatial distribution? Are these factors related to $PM_{2.5}$ and O_3 trade-offs or synergies? (2) How do the spatial characteristics of the two pollutants vary under the influence of trade-offs/synergies? This study can further strengthen understanding of the formation mechanisms and characteristics of combined $PM_{2.5}$ and O_3 pollution, especially in densely inhabited metropolitan regions with complex industrial structure and high environmental stress. The results provide valuable insights that support sustainable regional development.

2. Materials and Methods

2.1. Study Area

The Shenyang Metropolitan Area (SYMA) lies in the southern part of Northeast China (40°00′–43°49′N and 121°02′–125°79′E) and serves as an important population and economic agglomeration in Liaoning Province. With Shenyang as the core city, it extends to surrounding cities and the Shenyang-Fushun (Shenfu) Reform and Innovation Demonstration Zone (Figure 1). The area is characterized by a temperate continental monsoon climate, marked by four clearly differentiated seasons. In terms of geographical features, there is a lowland plain in the center and mountains and hills in the east and west. Owing to the influence of monsoon circulation, the annual average temperature decreases gradually from the southwest to the northeast and shows a decreasing trend from the plain to the mountainous areas. The temperature in the eastern mountainous area is lower than in the west. For annual precipitation, the overall trend gradually decreases from southeast to northwest. The Liao River, together with the Hun River, Taizi River, and other tributaries, forms the main hydrological system. Land use is characterized by cropland dominance in the plains, whereas the mountainous and hilly areas support higher forest cover. Since the establishment of the metropolitan area, the economy has grown rapidly, with a GDP exceeding 1.4 trillion yuan and a resident population of more than 23 million, underscoring its importance as a regional economic and demographic hub. The industrial structure of this region is characterized by heavy equipment, aerospace, automotive, and parts manufacturing, supplemented by modern service industries. In addition, steel smelting, petrochemical processing, and coal-fired power generation constitute important supporting industries. According to the Liaoning Statistical Yearbook (2023) and the China Ecological Environment Status Bulletin (2023), these sectors contribute a high proportion of regional emissions of NO_x, SO_2, and particulate matter, with the iron and steel industry and thermal power plants being the largest stationary sources [2,24]. The industrial characteristics of high energy consumption and high emissions have exacerbated the formation and diffusion

of complex air pollution. These typical industrial urban agglomeration characteristics make SYMA a suitable area for our research.

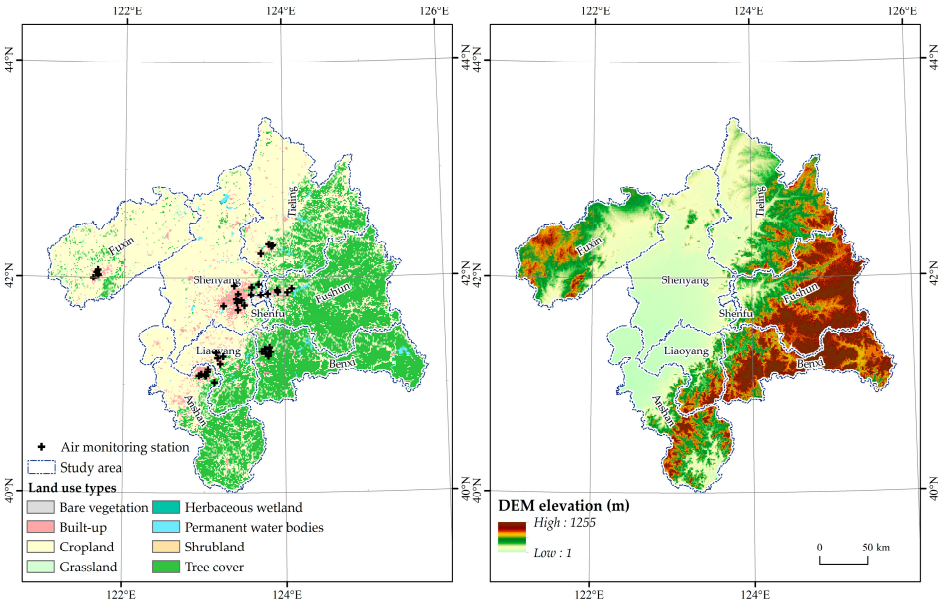


Figure 1. Study area of the Shenyang Metropolitan Area. The left panel shows the locations of air quality monitoring stations and the distribution of land use types, while the right panel presents the topography based on a Digital Elevation Model (DEM, in meters). The coordinate axes denote latitude and longitude (°).

2.2. Technique Route

To compare the trade-offs and synergies among the determinants of combined $PM_{2.5}$ and O_3 pollution, the study adopted an analytical framework consistent with previous research on $PM_{2.5}$ pollution [21]. First, pollutant concentration data were obtained from 43 air quality monitoring stations (Table S1). Missing values were interpolated in accordance with relevant standards, and the dataset was grouped by season to reflect the climatic characteristics of the study area. These data served as the dependent variables for subsequent modeling. Environmental data covering nine categories—including geographic information, population, roads, land use, building height, meteorological factors, vegetation index, atmospheric composition, and landscape metrics—were compiled to construct 34 independent variables (Table 1). Detailed variable definitions, abbreviations, and processing steps are included in the Supplementary Materials (Section S1). Second, the LUR models were then fitted using the LASSO algorithm to identify the most significant influencing predictors of O_3 pollution variations. The results were compared with earlier results for $PM_{2.5}$, enabling an assessment of the trade-offs and synergies between determinants of combined pollution. Third, pollution maps were generated from the model outputs to characterize the spatial patterns of combined $PM_{2.5}$–O_3 pollution across the SYMA.

Table 1. Overview of variables and associated data sources employed in the research.

Data Type	Variable	Source
Geographic information	Longitude Latitude	Geographic coordinate
	Elevation	Shuttle Radar Topography Mission (SRTM) digital elevation dataset Version 4, CGIAR-CSI, International Centre for Tropical Agriculture, Nairobi, Kenya.

Table 1. *Cont.*

Data Type	Variable	Source
Population	Population count	LandScan data by Oak Ridge National Laboratory (https://landscan.ornl.gov/, accessed on 20 February 2024)
Road data	Total road length within buffer radius Distance to the nearest road Distance to the nearest road intersection	Road vector data from Open Street Map (https://www.openstreetmap.org/, accessed on 2 January 2020)
Land use type	Cover ratio of 8 land use types (tree, shrubland, grassland, cropland, built-up, bare vegetation, permanent water bodies, and herbaceous wetland) within buffer radius	European Space Agency (ESA) WorldCover 10 m 2020 product, ESA WorldCover Consortium, Mol, Belgium.
Building height	Average building height within buffer radius	Chinese building height dataset CNBH-10m (https://zenodo.org/records/7923866, accessed on 5 January 2024)
Meteorological factor	Wind speed Surface net solar radiation Air temperature of 2 m Relative humidity Surface pressure	Daily meteorological data from the 5th ECMWF atmospheric reanalysis of global climate, Copernicus Climate Change Service (C3S) Climate Data Store (CDS), Reading, United Kingdom.
	Land surface temperature	8-day land surface temperature (LST) from MOD11A2 V6.1 product, NASA Land Processes Distributed Active Archive Center, Sioux Falls, United States.
Vegetation index	Normalized difference vegetation index	Normalized difference vegetation index (NDVI) from MOD13A2V6.1 product, NASA Land Processes Distributed Active Archive Center, Sioux Falls, United States.
Atmospheric composition	Aerosol optical depth	Aerosol optical depth (AOD) retrieved in the MODIS Blue band (0.47 μm) from MCD19A2 V6.1 product, NASA Land Processes Distributed Active Archive Center, Sioux Falls, United States.
	Total atmospheric column of ozone Tropospheric formaldehyde column number density Tropospheric nitrogen dioxide column number density	Sentinel-5 Precursor Offline (OFFL) datasets, Atmospheric Mission Performance Cluster (ATM-MPC) consortium, De Bilt, Netherlands.
Landscape metrics	Aggregation index within buffer radius Interspersion and juxtaposition index within buffer radius Splitting index within buffer radius Mean fractal dimension index within buffer radius Perimeter-area fractal dimension within buffer radius Large patch index within buffer radius Shannon's diversity index within buffer radius	Calculated based on 10 m land use data using the 'landscape-metrics' package in R.

2.3. LUR Modeling and Evaluation

In this study, the LASSO regression model was employed as the modeling approach. Compared with ordinary least squares, LASSO has the advantage of simultaneously estimating coefficients and performing variable selection, which is particularly useful in LUR models where predictors are often correlated. Moreover, given the relatively small number of monitoring stations (n = 43), complex ensemble algorithms such as random forest (RF) are prone to overfitting and may generate unstable results. Therefore, LASSO was selected as a robust machine learning method to fit the LUR model. LASSO extends the traditional linear regression model by adding a penalty term to the loss function, which constrains the sum of the absolute values of the regression coefficients. The optimization problem can be expressed as:

$$\hat{\beta} = \underset{\beta}{argmin}\left\{\sum_{i=1}^{n}\left(y_i - \beta_0 - \sum_{j=1}^{p}\beta_j x_{ij}\right)^2 + \lambda\sum_{j=1}^{p}|\beta_j|\right\}$$

where y_i is the dependent variable, x_{ij} represents independent variables, β_j denotes regression coefficients, and λ is a tuning parameter controlling the degree of shrinkage. When λ increases, less relevant predictors are forced toward zero, effectively performing variable selection. The 'glmnet' package in R was applied to perform the LASSO modeling [25]. Firstly, variables were normalized by z-score to prevent scale differences between data from causing a fitting bias. Leave-one-out cross validation (LOOCV) was adopted to evaluate the generalization ability of the models. The R^2 and root mean square error (RMSE) of LOOCV were reported as quantitative measures of the model's performance.

The assumption of residual normality was tested through Q–Q plots and the Shapiro–Wilk test, where the plots illustrate the alignment between empirical and theoretical quantiles under a normal distribution. If the residuals follow normality, the points should approximately fall along the 1:1 reference line, with only random scatter around it. The Shapiro–Wilk test statistically assesses normality, with *p*-values above 0.05 suggesting a normal distribution of data.

2.4. Pollution Surface Generation

Using annual and seasonal LUR models, 1 km-resolution pollution maps were constructed by combining grid-point variables with regression coefficients, followed by aggregation, reverse normalization, and rasterization in ArcGIS 10.8. Seasonal spatial variations in pollutant concentrations were thereby illustrated. The assessment of combined pollution levels was based on the Ambient Air Quality Standards (GB 3095–2012) and the WHO Global Air Quality Guide (2021) [26]. In these guidelines, the Air Quality Guideline (AQG) values represent the recommended limits, while the Interim Targets (IT) provide stepwise thresholds to guide gradual improvements in air quality. For $PM_{2.5}$, a threshold of 35 $\mu g/m^3$ was adopted, and an additional threshold of 45 $\mu g/m^3$ was established to account for the generally high concentrations in the study area. For O_3, the seasonal peak standards (AQG = 60 $\mu g/m^3$, IT-2 = 70 $\mu g/m^3$) were used. Based on these thresholds, three pollution levels—high, medium, and low—were finally defined for annual concentrations of both pollutants.

3. Results and Discussion

3.1. Descriptive Statistics

The O_3 concentration was highest in the summer and spring, with no statistically significant difference between the two seasons (one-way ANOVA with post hoc test, $p > 0.05$), while the O_3 concentration levels were similar and low in autumn and winter (Figure 2). This pattern is largely attributed to enhanced photochemical activity during the warm seasons when high solar radiation, longer sunshine duration, and elevated temperatures accelerate the photolysis of NO_2 and the production of radicals, thereby promoting O_3 formation [27,28]. In contrast, reduced solar radiation, a lower boundary layer height, and more frequent stagnant meteorological conditions in autumn and especially winter suppress photochemical reactions, leading to low O_3 concentration [29,30].

The peak concentration of $PM_{2.5}$ pollution occurred in winter, followed by spring, and the pollution level was lowest in summer. The concentration of pollutants differed significantly among the four seasons [21]. This seasonal pattern is strongly linked to the combined effects of emissions and meteorology. Winter heating activities and intensive coal combustion in northern China substantially increase primary particle and precursor emissions [31,32]. Furthermore, weak vertical mixing, temperature inversions, and low boundary-layer heights favor the accumulation of fine particles during the cold season [33]. In spring, resuspension of dust and regional transport also contribute to elevated $PM_{2.5}$, while in summer, stronger atmospheric convection, frequent precipitation, and more efficient wet scavenging processes contribute to the lowest $PM_{2.5}$ levels [34–36]. Taken together, these results indicate that O_3 and

$PM_{2.5}$ exhibit contrasting seasonal cycles in SYMA, driven by the interplay between emission sources, photochemical activity, and meteorological conditions.

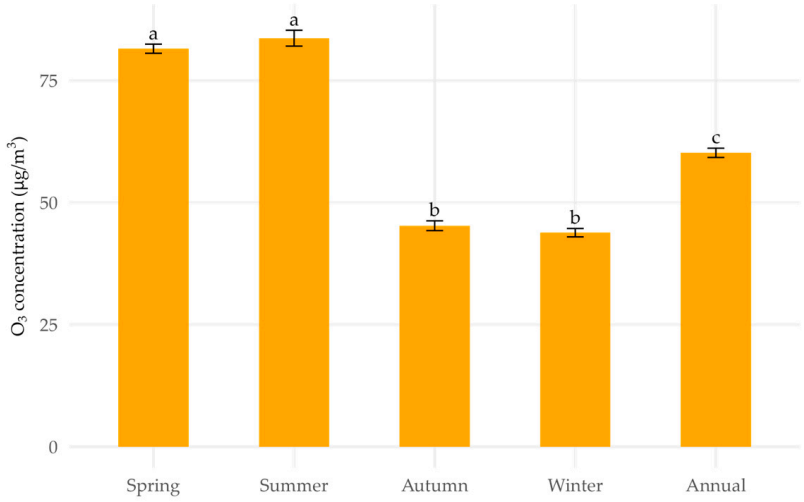


Figure 2. Seasonal and annual variations of O_3 concentrations (mean ± standard error). Different letters above the bars indicate significant differences among groups at $p < 0.05$.

In spring and summer, the O_3 concentrations in Fuxin were higher than those in other cities, which may be related to its geographic position in the northwestern part of the study area, where stronger solar radiation and relatively lower anthropogenic NO_x emissions reduce the titration of O_3 by NO, allowing photochemically produced O_3 to accumulate more efficiently. In contrast, Benxi consistently exhibited the lowest O_3 concentrations across all seasons, likely due to its location in the mountainous and forested southeastern region, where weaker solar radiation, complex terrain, and enhanced deposition associated with vegetation reduce surface O_3 levels. The average O_3 concentrations in other cities remained relatively similar, reflecting comparable emission and meteorological conditions within the central plain. However, the concentrations range in Fushun and Anshan showed relatively large fluctuations, suggesting the influence of local industrial emissions and complex topography on O_3 variability. These results highlight the combined roles of geographic setting, chemical regimes, and emission characteristics in shaping the spatial heterogeneity of O_3 pollution within the SYMA (Figure 3).

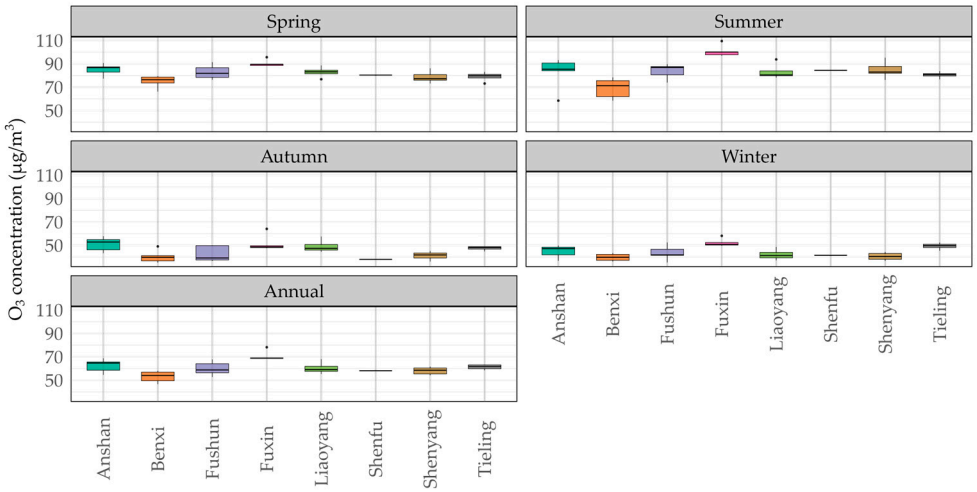


Figure 3. Seasonal and annual distributions of O_3 concentrations across the cities. The boxes represent the interquartile ranges (IQR), the horizontal line within each box indicates the median, whiskers denote the 1.5×IQR range, and individual points represent outliers beyond this range.

3.2. LUR Models of O_3

The variables of the O_3 LUR models explained 57–87% of the variations in concentrations, and the summer LUR model had the best fit (Table 2). The annual R_{cv}^2 value was 0.49, and the seasonal R_{cv}^2 values were 0.62–0.81. The annual average RMSE was 0.71 ug/m^3 and the seasonal RMSEs were 0.43–0.66 ug/m^3. The Q–Q plots (Figure 4) and Shapiro–Wilk test results (spring: p = 0.83; summer: p = 0.53; autumn: p = 0.37; winter: p = 0.50; annual average: p = 0.57) all indicated the effectiveness of the O_3 model and its ability to reproduce O_3 concentrations.

Table 2. The O_3 land use regression (LUR) model fit.

Model	Predictive Variable (Partial R^2, Positive/Negative Direction)	Adj. R^2	LOOCV	
			R_{cv}^2	RMSE
Annual	X (0.47, −), dist_road (0.11, +), Cropland_5000 (0.12, +), Permanent water bodies_100 (0.15, +)	0.57	0.49	0.71
Spring	X (0.45, −), pop_count (0.30, −), road_50 (0.20, +), dist_road (0.46, +), Tree_cover_100 (0.18, −), Cropland_500 (0.24, −), Grassland_500 (0.31, −), Permanent water bodies_100 (0.29, +), IJI_100 (0.29, −), SHDI_200 (0.18, +)	0.77	0.62	0.63
Summer	DEM (0.58, +), pop_count (0.30, −), dist_road (0.45, +), Built up_500 (0.56, +), Permanent water bodies_1000 (0.45, +), RH (0.81, −), FRAC_MN_5000 (0.19, −), IJI_1000 (0.14, −), LPI_2000 (0.15, −)	0.87	0.81	0.43
Autumn	dist_road (0.23, +), Cropland_5000 (0.20, +), RH (0.26, −), AOD (0.54, −), Permanent water bodies_100 (0.16, +), BH_50 (0.31, +), TEMP (0.18, +)	0.71	0.62	0.62
Winter	DEM (0.21, +), road_5000 (0.21, −), dist_road (0.10, +), Permanent water bodies_100 (0.19, +), RH (0.18, −), NO_2_TC (0.11, −), IJI_100 (0.26, −)	0.68	0.57	0.66

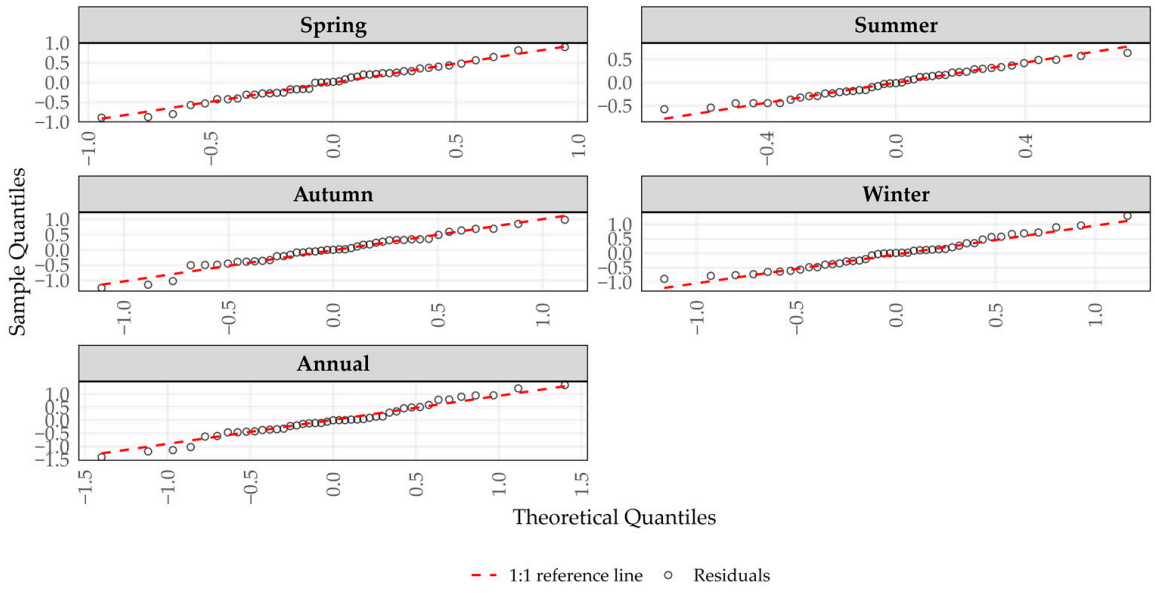


Figure 4. Q-Q plots of O_3 model residuals. Seasonal subsets (spring, summer, autumn, winter) and the annual aggregate are displayed. X-axis: Theoretical quantiles of a standard normal distribution (0,1); Y-axis: Sample quantiles of model residuals. Black points represent the standardized residuals, and the red dashed line indicates the 1:1 theoretical reference line. Deviations from this line suggest departures from residual normality.

In the spring model, the longitude (X, −) and distance to the nearest road (dist_road, +) were the main contributing factors. In summer, the main influential factor was relative humidity (RH, −). In autumn, the factor with the strongest influence was aerosol optical depth (AOD, −) in atmospheric components. In winter, the most significant factor affecting the spatial distribution difference of O_3 concentration was the interspersion and juxtaposition index within 100 m (IJI_100, −).

X was found to be negatively correlated with O_3 concentrations, which may be attributed to meteorological factors and vegetation conditions. The air humidity in the east of the research area was greater than in the west. Elevated relative humidity (RH, −) promotes O_3 reduction by enhancing dry deposition onto wet surfaces and suppresses photochemical production by scavenging radicals and shifting NO_x–VOC chemistry into the aqueous phase [37,38]. In addition, lower temperatures in the eastern mountainous area reduced the chemical reaction rate of O_3 formation, supporting the observed negative correlation between longitude and O_3 concentration.

A positive correlation between dist_road and O_3 concentration was consistently identified across all models. This can be explained by the near-road "NO titration effect," where freshly emitted NO consumes O_3, leading to lower roadside concentrations [39]. Moreover, the structures around roads, such as buildings, trees, and green belts, may affect solar radiation, thus reducing the intensity of photochemical reaction and resulting in a lower O_3 concentration near the road [14]. Furthermore, as the distance from roads increases, the concentration of O_3 may increase owing to the diffusion, mixing, and additional emissions of precursor pollutants.

In the autumn model, AOD emerged as the most influential factor, exerting a negative effect. As a measure of columnar aerosol extinction, AOD not only reflects aerosol loading but also plays a critical role in regulating atmospheric radiation balance and photochemical processes [40,41]. High aerosol burdens reduce surface ultraviolet radiation via scattering and absorption, which suppresses the photolysis of NO_2 and the production of radicals such as OH—both critical precursors for O_3 formation [27,42]. Deng et al. found that a high AOD concentration can lead to a reduction in surface ultraviolet radiation of more than 50%; this significant decrease in ultraviolet radiation will further reduce the photochemical productivity of O_3 [43]. This radiative effect, coupled with possible heterogeneous uptake of radicals on particle surfaces, helps explain the negative correlation between AOD and O_3.

In the winter model, the Interspersion and Juxtaposition index (IJI_100, −) was identified as the strongest factor. IJI is an "aggregation metric" (also called the "salt and pepper" metric) that describes the intermixing of landscape classes. Higher values indicate more diverse and spatially intermixed patterns [44]. Therefore, the results suggest that greater heterogeneity of different land use types at a local scale (100 m) within the city may help reduce O_3 concentrations. Previous urban ecology studies also highlight that landscape diversity enhances microclimatic regulation, mitigates heat island effects, and improves atmospheric mixing, which collectively contribute to lower pollutant accumulation [45–47]. This finding emphasizes the need to consider landscape diversity in urban planning to effectively address urban air pollution and improve the quality of life for residents.

3.3. Synergistic and Trade-Off Factors Affecting $PM_{2.5}$ and O_3

"Trade-off factors" in the study were factors that acted in opposite directions on $PM_{2.5}$ and O_3 concentrations, while "synergistic factors" were factors that acted in the same direction. Figure 5 shows the direction and frequency of each variable's impact in all O_3 models and in Shi et al.'s $PM_{2.5}$ models [21].

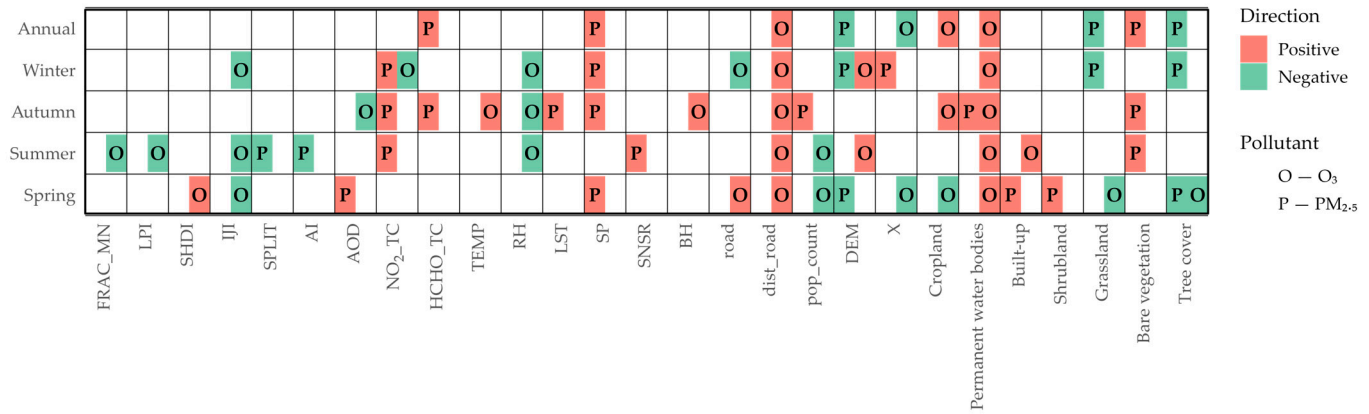


Figure 5. Directions of predictors in $PM_{2.5}$ and O_3 LUR models. Different colors show the positive and negative influence of directions. The letters P and O refer to the pollutants $PM_{2.5}$ and O_3, respectively.

The directions of Tree_cover, Grassland, Built_up, and Permanent_water_bodies in the land use-type variables were consistent on the two pollutants, showing synergistic effects. However, Tree_cover and Grassland alleviated the concentrations of the two pollutants, while Built_up and Permanent_water_bodies increased the concentrations of the two pollutants.

The directions of X and elevation (DEM), population count (pop_count), tropospheric nitrogen dioxide column number density (NO_2_TC), and AOD were opposite for the two pollutants, showing trade-off effects. Higher X, pop_count, NO_2_TC, and AOD in atmospheric constituent values led to a higher $PM_{2.5}$ concentration and a lower O_3 concentration. Higher elevation led to a lower $PM_{2.5}$ concentration and a higher O_3 concentration.

The mechanism of X's influence on O_3 concentration was analyzed in Section 3.2. The relationship between X and $PM_{2.5}$ concentration may be related to the seasonality of weather systems. The variable X was only selected as a predictor in the winter and annual models of $PM_{2.5}$, and the effect direction was positive, which meant that there were higher $PM_{2.5}$ concentrations in the east of SYMA [21]. According to Ma et al.'s research on the Liaoning central urban agglomeration, the prevailing northwest wind in winter can bring pollutants to the area [48]. The east of the research area is mountainous, and pollutants are easily blocked by the terrain to form accumulations. Similar studies have shown that complex topography tends to enhance pollutant stagnation under weak dispersion conditions, particularly during cold seasons when boundary layer height is low and atmospheric mixing is suppressed [49]. This might be the dominant reason explaining the models.

Elevation negatively affected $PM_{2.5}$ concentration. This may be because more elevated areas are often located farther from major anthropogenic emission sources and generally experience stronger atmospheric mixing and ventilation, which enhance pollutant dispersion. In contrast, the relatively high O_3 levels at higher elevations can be attributed to stronger ultraviolet radiation that accelerates the photochemical reactions of NO_x; and VOCs. Similar results were observed by Brodin et al. in the Colorado Front Range Mountains [50]. In addition, coupled with the long-distance transmission of pollution precursors, such as the wind-driven diffusion of pollutants from industrial areas and the combined effect of natural source VOCs, this led to a situation where $PM_{2.5}$ pollution was low in high-elevation areas, but O_3 was prone to accumulate and increase.

In the autumn model, pop_count was recognized as positively affecting $PM_{2.5}$ concentration. Ma et al. found that in the study area, local emissions in autumn were the main pollution source, unlike the particulate matter pollution of winter and spring, which is from external sources [48]. Pop_count reflected the intensity of population activity, and higher

population density implied stronger direct emissions from residential heating, cooking, traffic, and other anthropogenic activities, indirectly explaining the positive relationship between pop_count and $PM_{2.5}$ concentrations. In contrast, unlike $PM_{2.5}$, ground-level O_3 is mainly produced through photochemical reactions, making it a secondary pollutant. A pop_count with a 10 m spatial resolution represents the population micro-environmental population density, which usually indicates high building density, narrow street canyons, and poor ventilation conditions. Such conditions favor the accumulation of NO_x emissions from vehicles and domestic activities, enhancing O_3 titration by NO and thus reducing O_3 concentrations locally [51]. This mechanism helps explain the observed opposite relationships of pop_count with $PM_{2.5}$ (positive) and O_3 (negative).

The positive correlation between NO_2_TC in the atmospheric composition and the concentration of $PM_{2.5}$ meant that when the concentration of NO_2 increased, $PM_{2.5}$ concentrations also tended to increase. This may be attributed to their common emission sources between NO_2 and $PM_{2.5}$, such as vehicle exhaust and industrial emissions. Moreover, NO_2 can undergo oxidation in the atmosphere to form nitric acid, which then reacts with ammonia to produce ammonium nitrate, an important secondary inorganic component of $PM_{2.5}$ [52]. Studies have confirmed that NO_2 plays a crucial role in the formation of secondary aerosols, particularly ammonium nitrate, which contributes substantially to haze events in northern China [53,54]. The significant negative correlation between NO_2_TC and near-surface O_3 concentration appeared only in the winter model. In winter, weaker solar radiation reduces the photolysis rate of NO_2, limiting O_3 generation pathways [55]. Meanwhile, a shallow and stable boundary layer in winter inhibits the vertical diffusion, leading to high near-surface NO_2 concentrations. However, as NO_2_TC represents the column concentration, its surface contribution may be underestimated owing to dilution effects at higher altitudes. For example, observations in Beijing in winter showed that the near-surface NO_2 concentrations decrease by 60–80% with height, but the NO_2_TC retrieved by satellites could not distinguish the vertical gradients [56]. Similarly, unmanned aerial vehicle observations indicated that the near-surface O_3 is strongly suppressed by NO titration, while O_3 concentrations increase with altitude in winter due to reduced NO emissions aloft [57].

The reason why AOD was positively correlated with the concentration of near-surface $PM_{2.5}$ but negatively correlated with the concentration of O_3 can be explained by aerosol light extinction and its influence on photochemical processes. In the study area, $PM_{2.5}$ typically accounts for a substantial fraction of aerosol mass concentration and thus strongly contributes to columnar AOD, especially during haze episodes [58]. An increase in $PM_{2.5}$ mass leads to higher aerosol extinction, thereby elevating AOD values [59–61]. Under high-AOD conditions, aerosols weaken the ultraviolet radiation reaching the ground through scattering and absorption [17], reducing the photolysis rate of NO_2 and the free radicals (such as hydroxyl) required for O_3 formation. Simulations showed that when AOD increased from 0.8 to 2.0, the peak surface O_3 concentration dropped by 83% [62]. It should be noted, however, that this relationship depends on the composition and size distribution of aerosols: coarse-mode dust particles can also produce large extinction values, while black carbon has stronger absorption efficiency than sulfate or sea salt. Seasonal variation in aerosol types—for example, enhanced black carbon during the heating season or secondary organic aerosols in summer—may therefore modulate the magnitude of the observed AOD–$PM_{2.5}$–O_3 relationships. This highlights that the trade-off effect identified here represents the dominant local conditions, but its strength can vary with aerosol sources and composition.

Tree_cover and Grassland in land use types both had negative impacts on the concentrations of the two pollutants and played mitigating roles. The result confirms the

importance of vegetation in mitigating combined air pollution. Built_up and Permanent_water_bodies had positive effects on the rise in the concentration of two pollutants. The expansion of the built-up area is usually accompanied by an increase in industrial activities, traffic flow, and energy consumption. Many studies have found a significant positive correlation between the proportion of built-up area and the concentration of $PM_{2.5}$, which is mainly attributed to industrial pollution source emissions, motor vehicle exhaust, and construction dust [63]. The studies also found that the layout of buildings in urban areas affected pollutant diffusion and that increased urban compactness can intensify pollutant retention [64,65]. A high proportion of built-up area often corresponds to higher population density and energy consumption. For instance, a geographically weighted regression model indicated that industrial activities, per capita GDP and $PM_{2.5}$ concentration were significantly correlated, especially in northern cities where the demand for winter heating aggravated pollution [64]. The correlation between Built_up and O_3 in our model exhibited seasonal differences. In summer, there was a strong positive correlation, while in autumn and winter, the correlations were negative (Figures S1–S4). This highlights that the urban heat island effect has a seasonal impact on pollutant production. In addition, although we found a positive correlation between built-up area and the pollution intensity of O_3, the relationship exhibits different trends and strengths in urban agglomerations with varying geographic areas, degrees of development, and ecological backgrounds [66]. This reflects that Built_up has a complex relationship with the synergistic effect of the two pollutants, and the mechanism requires further research.

The permanent water body cover ratio (Permanent_water_bodies) had a positive correlation with the two pollutants in all five O_3 models. This may be attributed to several empirically supported mechanisms. First, water bodies often have low surface reflectance and high specific heat, leading to elevated local temperatures that prolong the window for photochemical O_3 production [67]. Microclimate simulation studies have demonstrated that biogenic VOC emissions—particularly isoprene—substantially increase under such heat-driven conditions, which can significantly elevate O_3 concentrations in NO_x-rich environments [68]. Second, extensive water surfaces contribute to higher ambient humidity. Elevated humidity and aerosol liquid water content promote heterogeneous and aqueous-phase reactions of gaseous precursors (e.g., SO_2, NO_x, NH_3), thereby accelerating the formation of secondary aerosols like sulfates, nitrates, and organic oxidation products. Field studies have confirmed that aerosol water significantly enhances secondary aerosol production under humid conditions [69,70]. In addition, the selection of this variable in the autumn $PM_{2.5}$ model may reflect autumn-specific meteorological stability intensified by local water bodies, which enhance the residence time of pollutants. However, the studies of Wu and Shi et al. indicated that the correlations between water body variables and these two pollutants could be both positive and negative [14,65]. This may be related to multiple factors in the study area, such as geographical location, season, area, and the mobility of water bodies [71], and the specific mechanisms require further exploration.

Our results share several common determinants with the PRD study by Wu et al. (2021)—including longitude, AOD, NO_2_TC, and population size—as well as trade-off effects between $PM_{2.5}$ and O_3 [14]; however, two notable differences emerge. First, the direction of the longitude effect is reversed in the SYMA. In SYMA, longitude covaries with topography and land use because of more mountainous and forested areas to the east, as well as a cooler and more humid microclimate, which jointly reduce photolysis rates and boundary-layer mixing and thereby depress O_3, while $PM_{2.5}$ can remain elevated under stable conditions. By contrast, the PRD is coastal, low-latitude, and strongly influenced by sea-breeze circulations and intense solar radiation, favoring more active photochemistry and a different east–west gradient in precursors and ventilation. Second, Wu et al. reported

trade-off effects for forest and grassland, whereas in SYMA these land use types exhibit synergistic mitigating effects on combined $PM_{2.5}$-O_3 pollution. This contrast can be attributed to differences in tree species and to the relatively low levels of biogenic VOC emissions in SYMA. Because biogenic VOC release is largely driven by temperature and solar radiation, the cooler local climate suppresses emissions. As a result, the "biogenic-VOC-driven O_3 enhancement" commonly reported in warmer, high-NO_x regions is much weaker in this study area. In addition, AOD and NO_2_TC remain trade-off factors in both regions. Regional differences in emission profiles (e.g., heating and heavy industry in SYMA versus the coastal industrial–transport mix in PRD), coupled with distinct chemical regimes and meteorological conditions, account for why the same predictors exhibit different effects or varying synergy–trade-off patterns across regions.

3.4. Spatial Pollution Maps

The predicted O_3 concentrations for spring, summer, autumn, winter, and annual average were 21.86–134.19 μg/m^3, 25.71–157.36 μg/m^3, 18.99–78.32 μg/m^3, 12.37–68.82 μg/m^3, and 48.54–89.75 μg/m^3, respectively. The predicted annual pollution concentration was higher in the west and lower in the east. Because the two predictive variables, dist_road and Permanent_water_bodies, were included in all models and their impact directions were both positive, the characteristics of low O_3 concentration along the road network and high concentration in the region of water bodies appeared, particularly in summer and spring (Figure 6).

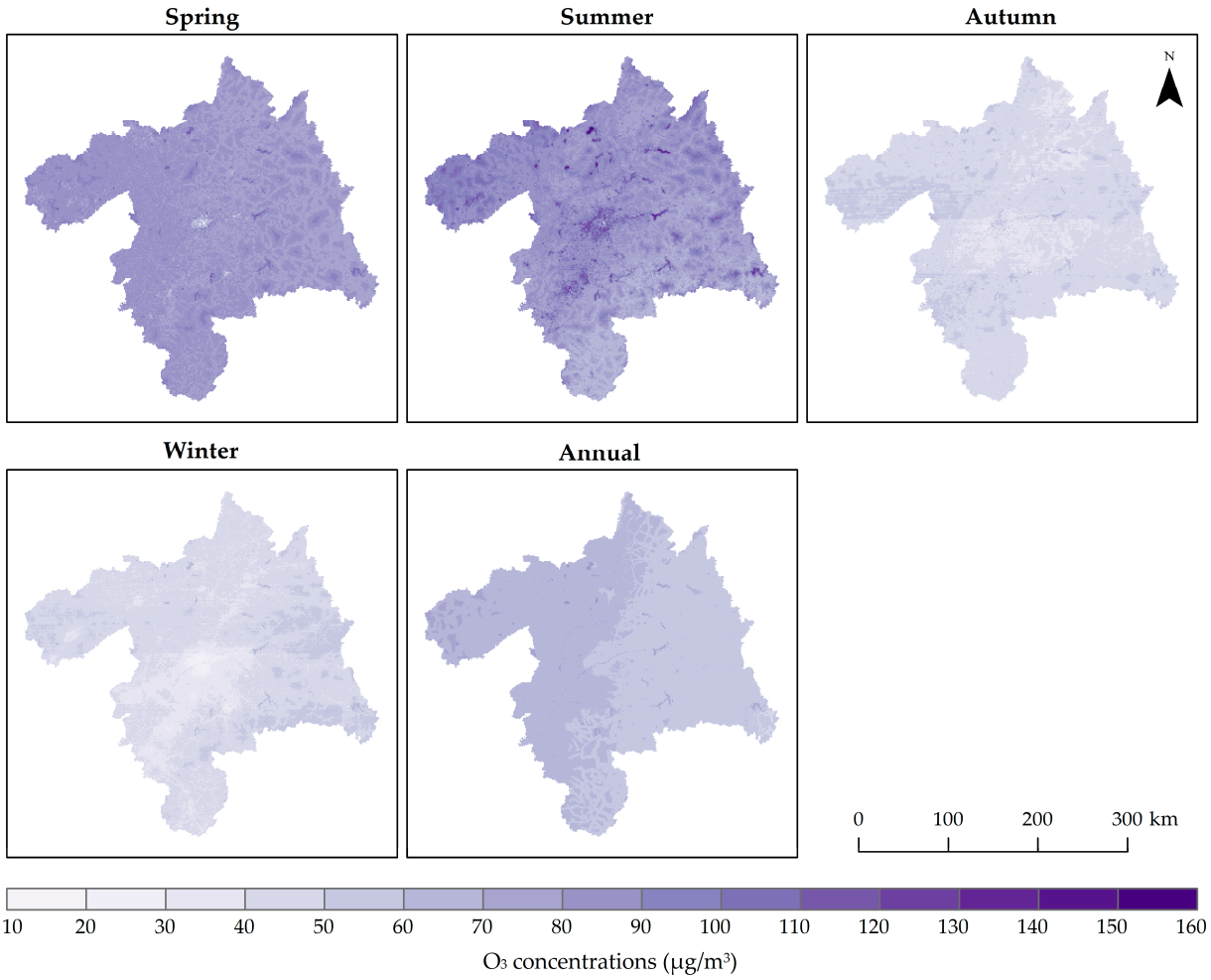


Figure 6. Spatial distribution of O_3 concentrations across seasons and the annual average. The color bar indicates O_3 concentration (μg/m^3), enabling direct interpretation of the spatial concentration gradients.

The seasons with the most $PM_{2.5}$ and O_3 pollution were completely different, in that $PM_{2.5}$ levels were higher in winter while O_3 levels were higher in spring and summer. To understand the overall pollution conditions, the annual $PM_{2.5}$ and O_3 pollution maps were selected for assessment (Figure 7). According to the principles of pollution level classification in Section 2.4, the two target pollutants were classified into three pollution grades: high, medium, and low. In Figure 7, the red color indicates the areas where the pollution level of $PM_{2.5}$ was relatively higher than that of O_3, with an area proportion of 46.97%; the gray color represents the pollution grades where $PM_{2.5}$ and O_3 were comparable, with an area proportion of 48.75%; the green color indicates the areas where the pollution level of O_3 was relatively higher than that of $PM_{2.5}$, with an area proportion of 4.27%. Whether in terms of spatial distribution characteristics or statistical data, the trade-off effect of combined pollution in the study area was dominated by higher $PM_{2.5}$, especially in the central plain area. In the west of Fuxin and a few areas in the south-central part of Anshan, O_3 pollution was dominant. Approximately 22.02% of the area had low levels of both $PM_{2.5}$ and O_3, mainly distributed in the east of the study area, which is mountainous and forested. The overlapping area with high values of the two pollutants was rare, accounting for 0.38% of the total area.

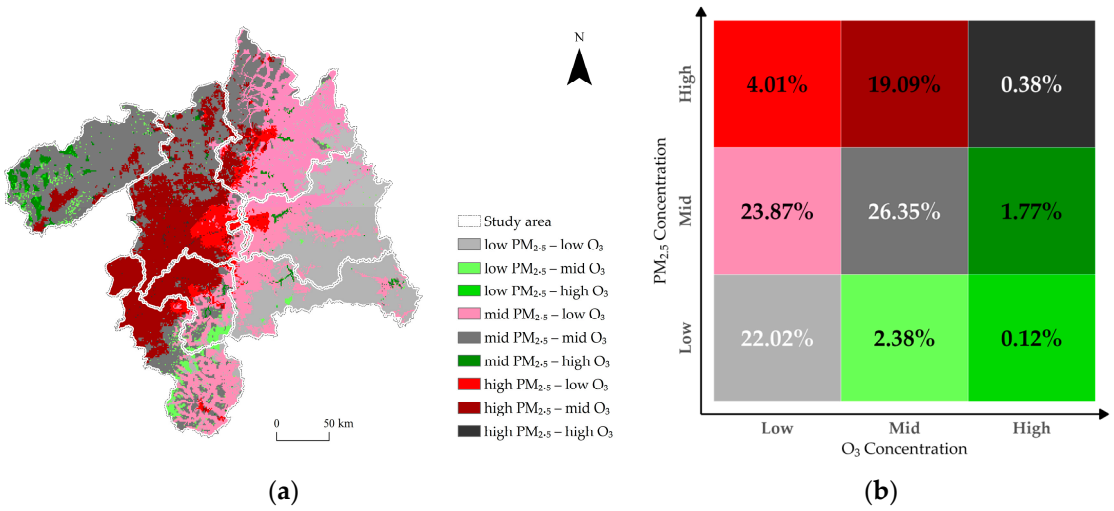


Figure 7. Comprehensive evaluation of combined $PM_{2.5}$-O_3 pollution levels (**a**) and area proportion statistics (**b**).

3.5. Recommendations and Limitations

Based on the synergy and trade-off factors identified in the study, several targeted recommendations for air quality management can be drawn. First, the synergistic mitigation effects of tree cover and grassland emphasize the role of vegetation planning in urban centers and downwind industrial zones, where both $PM_{2.5}$ and O_3 are elevated. Second, the trade-off role of NO_2 and aerosol optical depth (AOD) suggests that coordinated emission control of NO_x and VOCs, particularly in transportation hubs and industrial clusters, is crucial for addressing compound pollution. Third, the positive correlation between permanent water bodies and pollutants highlights the necessity of emission regulation in their vicinity to prevent secondary aerosol formation. Together, these insights refine existing policy frameworks by providing quantitative, spatially explicit evidence that can inform differentiated management in the Shenyang Metropolitan Area and similar regions.

We recognize that this study has certain limitations. First, we referred to the method of Wu et al. and judged the trade-offs and synergistic effects among influencing factors by analyzing the occurrence times and action directions of predictive variables in the models of the four seasons and the annual average in the study area [14]. However, we also noticed

that most variables had different seasonal contributions to pollutants, and in some cases, the action directions were even the opposite. Therefore, our results may only reflect the general rules and characteristics of this area. The action mechanisms for other study areas and specific influencing factors need further exploration. Additionally, considering that the LASSO algorithm is suitable for handling multi-dimensional data with a relatively small sample size and provides good interpretability, we chose this algorithm for model fitting in this study. Nevertheless, the LASSO algorithm assumes linear relationships between variables, which may oversimplify the complex and potentially non-linear atmospheric processes involved in pollutant formation and dispersion. In future research, more advanced non-linear machine learning methods should be considered to capture these complex interactions more comprehensively. Another potential limitation of this study is that model performance was evaluated only through LOOCV. Although LOOCV provides an unbiased internal validation for small datasets, the use of an independent external dataset would further strengthen model reliability and assess temporal transferability. However, the present study was based exclusively on monitoring data for 2020. Future work will address this limitation by incorporating data from adjacent years, thereby providing a more comprehensive evaluation of the generalizability of the models.

4. Conclusions

This study took the SYMA as the study area and used the LASSO algorithm to fit the LUR models of O_3, comparing the results with our previous study on $PM_{2.5}$ pollutants. We used the same research workflow to identify the key factors influencing the trade-off and synergistic effects of compound pollution. The main findings were as follows: (1) Among the land use-type variables, forest land, grassland, construction land, and water bodies showed a synergistic effect on the two pollutants, but in different directions. Forest land and grassland alleviated the concentrations of both pollutants, while construction land and water bodies contributed to an increase in the concentrations of both pollutants. (2) The longitude and elevation in the geographical location variables, population size, and NO_2 column density and aerosol optical depth in the atmospheric composition variables had opposite effects on the two pollutants, indicating a trade-off effect. (3) In terms of spatial distribution, the trade-off effect of compound pollution was dominated by $PM_{2.5}$ pollution, which was particularly prominent in the central plain area. In contrast, the eastern mountainous and forested areas had the least severe compound pollution.

Supplementary Materials: The following supporting information can be downloaded at https://www.mdpi.com/article/10.3390/su17178046/s1: Section S1: Land use regression (LUR) model variables; Table S1: List of coordinates of monitoring stations; Table S2: Description and abbreviations of environmental variables; Figure S1: Correlation matrix of O3 concentrations with independent variables in the spring land use regression (LUR) model, with grid colors indicating correlation coefficients; Figure S2: Correlation matrix of O3 concentrations with independent variables in the summer land use regression (LUR) model, with grid colors indicating correlation coefficients; Figure S3: Correlation matrix of O3 concentrations with independent variables in the autumn land use regression (LUR) model, with grid colors indicating correlation coefficients; Figure S4: Correlation matrix of O3 concentrations with independent variables in the winter land use regression (LUR) model, with grid colors indicating correlation coefficients; Figure S5: Correlation matrix of O_3 concentrations with independent variables in the annual land use regression (LUR) model, with grid colors indicating correlation coefficients.

Author Contributions: Conceptualization, T.S. and C.L.; methodology, T.S., X.Y., and F.L.; software, T.S.; formal analysis, T.S. and X.Y.; writing—original draft preparation, T.S. and X.Y.; writing—review

and editing, T.S. and C.L.; project administration, T.S.; funding acquisition, T.S. All authors have read and agreed to the published version of the manuscript.

Funding: This work was supported by the National Natural Science Foundation of China (No. 32301378), Liaoning Province College Students' Innovative Entrepreneurial Training Plan Program (No. S202410166025), Basic Scientific Research Project of the Educational Department of Liaoning Province (No. LJ242510166002), Major Incubation Project of Shenyang Normal University (No. ZD202301), and Doctoral Start-up Foundation of Shenyang Normal University (No. BS202114).

Institutional Review Board Statement: Not applicable.

Informed Consent Statement: Not applicable.

Data Availability Statement: Data are contained within the article and Supplementary Materials.

Conflicts of Interest: The authors declare no conflicts of interest.

Abbreviations

The following abbreviations are used in this manuscript. For more detailed abbreviations of the variables in the model, please refer to Table S2 in the Supplementary Materials.

LUR	Land use regression
SYMA	Shenyang metropolitan area
PRD	Pearl River delta
AQG	Air quality guideline
LASSO	Least absolute shrinkage and selection operator
VOCs	Volatile organic compounds
LOOCV	Leave-one-out cross validation
AOD	Aerosol optical depth

References

1. Hua, C.; Jiang, Q.; Chi, X.; Liu, C. Meteorological characteristics of PM2.5–O_3 air combined pollution in central and Eastern China in the summer half years of 2015–2020. *Res. Environ. Sci.* **2022**, *35*, 650–658.
2. Ministry of Ecology and Environment of China (MEE). *Report on the State of the Ecology and Environment in China 2023*; Ministry of Ecology and Environment of the People's Republic of China: Beijing, China, 2024.
3. Lelieveld, J.; Haines, A.; Burnett, R.; Tonne, C.; Klingmüller, K.; Münzel, T.; Pozzer, A. Air pollution deaths attributable to fossil fuels: Observational and modelling study. *BMJ* **2023**, *383*, e077784. [CrossRef]
4. Zaręba, Ł.; Piszczatowska, K.; Dżaman, K.; Soroczynska, K.; Motamedi, P.; Szczepański, M.J.; Ludwig, N. The Relationship between Fine Particle Matter (PM2.5) Exposure and Upper Respiratory Tract Diseases. *J. Pers. Med.* **2024**, *14*, 98. [CrossRef]
5. Feng, Y.; Castro, E.; Wei, Y.; Jin, T.; Qiu, X.; Dominici, F.; Schwartz, J. Long-term exposure to ambient PM2.5, particulate constituents and hospital admissions from non-respiratory infection. *Nat. Commun.* **2024**, *15*, 1518. [CrossRef] [PubMed]
6. Curtis, L. PM2.5, NO_2, wildfires, and other environmental exposures are linked to higher COVID 19 incidence, severity, and death rates. *Environ. Sci. Pollut. Res.* **2021**, *28*, 54429–54447. [CrossRef] [PubMed]
7. Fu, C.-B.; Tang, J.-X.; Dan, L.; Tong, J.-H. Characteristics, Impact Factors and Potential Sources of PM2.5 Pollution for Hainan Island. *Huan Jing Ke Xue=Huanjing Kexue* **2024**, *45*, 5140–5148.
8. Shi, B.; Liu, G.; Fu, J.; Zhai, S.; He, L.; Li, R.; Chen, W. Traceability and policy suggestions for ozone pollution in heavy industrial city in Northeast China. *Environ. Sci. Pollut. Res.* **2024**, *31*, 47630–47643. [CrossRef]
9. Kim, S.; Yi, S.M.; Park, J.M.; Song, I.H.; Jeon, K.; Park, J. Simultaneous comparison of the chemical composition and attributable source of PM2.5 during 2014–2018 in major metropolitan cities in South Korea: Impacts of policy interventions. *Environ. Res. Lett.* **2024**, *19*, 114020. [CrossRef]
10. Zhang, J.K.; Su, Y.F.; Chen, C.Y.; Guo, W.K.; Tan, Q.W.; Feng, M.; Song, D.L.; Jiang, T.; Chen, Q.; Li, Y.; et al. Chemical composition, sources and formation mechanism of urban PM2.5 in Southwest China: A case study at the beginning of 2023. *Atmos. Chem. Phys.* **2024**, *24*, 2803–2820. [CrossRef]
11. Wang, H.; Sun, Y.; Dong, F. Insight into the Overlooked Photochemical Decomposition of Atmospheric Surface Nitrates Triggered by Visible Light. *Angew. Chem. Int. Ed.* **2022**, *61*, e202209201. [CrossRef]
12. Chen, Q.; Fang, Y.; Feng, Y.; Zhang, F.; Zhu, W.; Wang, W.; Chen, Y. Based on the variation of black carbon in PM2.5 to observe pollution episode in winter Shanghai. *J. Shanghai Univ. (Nat. Sci. Ed.)* **2020**, *26*, 263–274.

13. Liang, L.; Gong, P. Urban and air pollution: A multi-city study of long-term effects of urban landscape patterns on air quality trends. *Sci. Rep.* **2020**, *10*, 18618. [CrossRef]
14. Wu, J.; Wang, Y.; Liang, J.; Yao, F. Exploring common factors influencing PM 2.5 and O_3 concentrations in the Pearl River Delta: Tradeoffs and synergies. *Environ. Pollut.* **2021**, *285*, 117138. [CrossRef]
15. Du, S.W.; He, C.; Zhang, L.; Zhao, Y.; Chu, L.L.; Ni, J.M. Policy implications for synergistic management of PM 2.5 and O_3 pollution from a pattern-process-sustainability perspective in China. *Sci. Total Environ.* **2024**, *916*, 170210. [CrossRef]
16. Curley, L.; Holland, R.; Khan, M.A.H.; Shallcross, D.E. Investigating the Effect of Fine Particulate Matter (PM 2.5) Emission Reduction on Surface-Level Ozone (O_3) during Summer across the UK. *Atmosphere* **2024**, *15*, 733. [CrossRef]
17. Shao, P.; Xin, J.; An, J.; Wang, J.; Wu, F.; Wang, Y. An analysis on the relationship between ground-level ozone and particulate matter in an industrial area in the Yangtze River Delta during summer time. *Chin. J. Atmos. Sci.* **2017**, *41*, 618–628.
18. Wang, C.; Wang, S.; Yang, B.; Zhang, L.; Wang, L.; Liu, M. Study of the effect of meteorological conditions on the ambient air ozone concentrations in Shenyang. *Environ. Monit. China* **2015**, *31*, 32–37.
19. Ndiaye, A.; Shen, Y.; Kyriakou, K.; Karssenberg, D.; Schmitz, O.; Flückiger, B.; Hoogh, K.d.; Hoek, G. Hourly land-use regression modeling for NO_2 and PM 2.5 in the Netherlands. *Environ. Res.* **2024**, *256*, 119233. [CrossRef]
20. Ma, X.; Zou, B.; Deng, J.; Gao, J.; Longley, I.; Xiao, S.; Guo, B.; Wu, Y.; Xu, T.; Xu, X.; et al. A comprehensive review of the development of land use regression approaches for modeling spatiotemporal variations of ambient air pollution: A perspective from 2011 to 2023. *Environ. Int.* **2024**, *183*, 108430. [CrossRef]
21. Shi, T.; Zhang, Y.; Yuan, X.; Li, F.; Yan, S. Spatial Patterns and Determinants of PM 2.5 Concentrations: A Land Use Regression Analysis in Shenyang Metropolitan Area, China. *Sustainability* **2024**, *16*, 5119. [CrossRef]
22. Sun, Y.; Luo, Z.; Fan, X. Robust structured heterogeneity analysis approach for high-dimensional data. *Stat. Med.* **2022**, *41*, 3229–3259. [CrossRef] [PubMed]
23. Coker, E.S.; Amegah, A.K.; Mwebaze, E.; Ssematimba, J.; Bainomugisha, E. A land use regression model using machine learning and locally developed low cost particulate matter sensors in Uganda. *Environ. Res.* **2021**, *199*, 111352. [CrossRef]
24. Liaoning Provincial Bureau of Statistics. *Liaoning Statistical Yearbook 2023*; Liaoning Statistical Bureau: Shenyang, China, 2023.
25. Friedman, J.; Hastie, T.; Tibshirani, R. Regularization paths for generalized linear models via coordinate descent. *J. Stat. Softw.* **2010**, *33*, 1. [CrossRef] [PubMed]
26. Ministry of Ecology and Environment of China (MEE). *Ambient Air Quality Standards (GB 3095–2012)*; China Environmental Science Press: Beijing, China, 2012.
27. Li, K.; Jacob, D.J.; Liao, H.; Shen, L.; Zhang, Q.; Bates, K.H. Anthropogenic drivers of 2013–2017 trends in summer surface ozone in China. *Proc. Natl. Acad. Sci. USA* **2019**, *116*, 422–427. [CrossRef] [PubMed]
28. Hu, F.; Xie, P.H.; Xu, J.; Lv, Y.S.; Zhang, Z.D.; Zheng, J.Y.; Tian, X. Long-term trends of ozone in the Yangtze River Delta, China: Spatiotemporal impacts of meteorological factors, local, and non-local emissions. *J. Environ. Sci.* **2025**, *156*, 408–420. [CrossRef]
29. Lu, X.; Hong, J.; Zhang, L.; Cooper, O.R.; Schultz, M.G.; Xu, X.; Wang, T.; Gao, M.; Zhao, Y.; Zhang, Y. Severe Surface Ozone Pollution in China: A Global Perspective. *Environ. Sci. Technol. Lett.* **2018**, *5*, 487–494. [CrossRef]
30. Wang, W.J.; Parrish, D.D.; Wang, S.W.; Bao, F.X.; Ni, R.J.; Li, X.; Yang, S.D.; Wang, H.L.; Cheng, Y.F.; Su, H. Long-term trend of ozone pollution in China during 2014–2020: Distinct seasonal and spatial characteristics and ozone sensitivity. *Atmos. Chem. Phys.* **2022**, *22*, 8935–8949. [CrossRef]
31. Qi, X.; Han, Y.; Che, H.; Zhou, J.; Peng, C.; Bao, Z.; Liu, Y.; Meng, L.; Zhang, S.; Yang, F.; et al. Characteristics and health risks assessment of PM 2.5-bound heavy metals during winter in urban areas of northern China: A case study in Kaifeng. *Sci. Total Environ.* **2024**, *955*, 177050. [CrossRef]
32. Liu, P.; Zhang, C.; Xue, C.; Mu, Y.; Liu, J.; Zhang, Y.; Tian, D.; Ye, C.; Zhang, H.; Guan, J. The contribution of residential coal combustion to atmospheric PM 2.5 in northern China during winter. *Atmos. Chem. Phys.* **2017**, *17*, 11503–11520. [CrossRef]
33. Zheng, G.J.; Duan, F.K.; Su, H.; Ma, Y.L.; Cheng, Y.; Zheng, B.; Zhang, Q.; Huang, T.; Kimoto, T.; Chang, D.; et al. Exploring the severe winter haze in Beijing: The impact of synoptic weather, regional transport and heterogeneous reactions. *Atmos. Chem. Phys.* **2015**, *15*, 2969–2983. [CrossRef]
34. Hu, W.Y.; Zhao, T.L.; Bai, Y.Q.; Kong, S.F.; Xiong, J.; Sun, X.Y.; Yang, Q.J.; Gu, Y.; Lu, H.C. Importance of regional PM 2.5 transport and precipitation washout in heavy air pollution in the Twain-Hu Basin over Central China: Observational analysis and WRF-Chem simulation. *Sci. Total Environ.* **2021**, *758*, 143710. [CrossRef]
35. Li, Y.; Zhou, L.; Liu, H.F.; Liu, S.; Feng, M.; Song, D.L.; Tan, Q.W.; Jiang, H.B.; Zuoqiu, S.; Yang, F.M. Disparities in precipitation effects on PM 2.5 mass concentrations and chemical compositions: Insights from online monitoring data in Chengdu. *J. Environ. Sci.* **2025**, *156*, 421–434. [CrossRef]
36. Liu, W.J.; Yu, Y.; Li, M.; Yu, H.K.; Shi, M.M.; Cheng, C.; Hu, T.P.; Mao, Y.; Zhang, J.Q.; Liang, L.L.; et al. Bioavailability and regional transport of PM 2.5 during heavy haze episode in typical coal city site of Fenwei Plain, China. *Environ. Geochem. Health* **2023**, *45*, 1933–1949. [CrossRef]

37. Belan, B.D.; Savkin, D.E. The Role of Air Humidity in Variations in Near-Surface Ozone Concentration. *Atmos. Ocean. Opt.* **2019**, *32*, 586–589. [CrossRef]
38. Clifton, O.E.; Fiore, A.M.; Massman, W.J.; Baublitz, C.B.; Coyle, M.; Emberson, L.; Fares, S.; Farmer, D.K.; Gentine, P.; Gerosa, G.; et al. Dry Deposition of Ozone Over Land: Processes, Measurement, and Modeling. *Rev. Geophys.* **2020**, *58*, e2019RG000670. [CrossRef]
39. Badia, A.; Vidal, V.; Ventura, S.; Curcoll, R.; Segura, R.; Villalba, G. Modelling the impacts of emission changes on O_3 sensitivity, atmospheric oxidation capacity, and pollution transport over the Catalonia region. *Atmos. Chem. Phys.* **2023**, *23*, 10751–10774. [CrossRef]
40. Chen, H.M.; Zhuang, B.L.; Liu, J.E.; Zhou, Y.N.; Hu, Y.X.; Chen, Y.; Gao, Y.M.; Wei, W.; Lin, H.J.; Li, S.; et al. Absorbing Aerosol Optical Properties and Radiative Effects on Near-Surface Photochemistry in East Asia. *Remote Sens.* **2023**, *15*, 2779. [CrossRef]
41. Akinyoola, J.A.; Oluleye, A.; Gbode, I.E. A Review of Atmospheric Aerosol Impacts on Regional Extreme Weather and Climate Events. *Aerosol Sci. Eng.* **2024**, *8*, 249–274. [CrossRef]
42. Ivatt, P.D.; Evans, M.J.; Lewis, A.C. Suppression of surface ozone by an aerosol-inhibited photochemical ozone regime. *Nat. Geosci.* **2022**, *15*, 536–540. [CrossRef]
43. Deng, X.; Zhou, X.; Wu, D.; Tie, X.; Tan, H.; Li, F.; Bi, X.; Deng, T.; Jiang, D. Effect of atmospheric aerosol on surface ozone variation over the Pearl River Delta region. *Sci. China Earth Sci.* **2011**, *54*, 744–752. [CrossRef]
44. Hesselbarth, M.H.K.; Sciaini, M.; With, K.A.; Wiegand, K.; Nowosad, J. landscapemetrics: An open-source R tool to calculate landscape metrics. *Ecography* **2019**, *42*, 1648–1657. [CrossRef]
45. Sohrab, S.; Csikós, N.; Szilassi, P. Landscape Metrics as Ecological Indicators for PM 10 Prediction in European Cities. *Land* **2024**, *13*, 2245. [CrossRef]
46. Hu, H.; Zeng, S.; Han, X. Effects of Urban Landscapes on Pollutant Concentrations in Chengdu Plain Urban Agglomeration. *Atmosphere* **2022**, *13*, 1492. [CrossRef]
47. Łowicki, D. Landscape pattern as an indicator of urban air pollution of particulate matter in Poland. *Ecol. Indic.* **2019**, *97*, 17–24. [CrossRef]
48. Ma, Y.; Zhao, H.; Liu, Q. Characteristics of PM 2.5 and PM 10 pollution in the urban agglomeration of Central Liaoning. *Urban. Clim.* **2022**, *43*, 101170. [CrossRef]
49. Zhong, J.; Zhang, X.; Wang, Y.; Wang, J.; Shen, X.; Zhang, H.; Wang, T.; Xie, Z.; Liu, C.; Zhang, H.; et al. The two-way feedback mechanism between unfavorable meteorological conditions and cumulative aerosol pollution in various haze regions of China. *Atmos. Chem. Phys.* **2019**, *19*, 3287–3306. [CrossRef]
50. Brodin, M.; Helmig, D.; Oltmans, S. Seasonal ozone behavior along an elevation gradient in the Colorado Front Range Mountains. *Atmos. Environ.* **2010**, *44*, 5305–5315. [CrossRef]
51. Shi, Y.; Lau, K.K.L.; Ng, E. Developing Street-Level PM 2.5 and PM 10 Land Use Regression Models in High-Density Hong Kong with Urban Morphological Factors. *Environ. Sci. Technol.* **2016**, *50*, 8178–8187. [CrossRef] [PubMed]
52. Wang, S.; Wang, Q.Y.; Zhang, T.; Liu, S.X.; Ho, S.S.H.; Tian, J.; Su, H.; Zhang, Y.; Wang, L.Y.; Wu, T.T.; et al. Elaborations of the influencing factors on the formation of secondary inorganic aerosols in a heavily polluted urban area of China. *J. Environ. Sci.* **2024**, *138*, 406–417. [CrossRef]
53. Zhang, R.; Sun, X.; Shi, A.; Huang, Y.; Yan, J.; Nie, T.; Yan, X.; Li, X. Secondary inorganic aerosols formation during haze episodes at an urban site in Beijing, China. *Atmos. Environ.* **2018**, *177*, 275–282. [CrossRef]
54. Zhai, S.X.; Jacob, D.J.; Wang, X.; Liu, Z.R.; Wen, T.X.; Shah, V.; Li, K.; Moch, J.M.; Bates, K.H.; Song, S.J.; et al. Control of particulate nitrate air pollution in China. *Nat. Geosci.* **2021**, *14*, 389–395. [CrossRef]
55. Afonso, N.F.; Pires, J.C.M. Characterization of Surface Ozone Behavior at Different Regimes. *Appl. Sci.* **2017**, *7*, 944. [CrossRef]
56. Zhang, Y.; Wei, Y.; de Leeuw, G.; Liu, O.; Chen, Y.; Lv, Y.; Zhang, Y.; Li, Z. Relation between total-column and near-surface NO_2 based on in-situ and PANDORA ground-based remote sensing observations. *EGUsphere* **2025**, *2025*, 1–35. [CrossRef]
57. Dai, S.; Zhou, C.; Pang, X.; Li, J.; Chen, L.; Wu, Z.; Yuan, K.; Han, Z.; Wang, Q.; Wang, S.; et al. Vertical profiles characteristics of near surface layer ozone in Shangyu Economic Development Zone of Hangzhou Bay based on unmanned aerial vehicle. *China Environ. Sci.* **2022**, *42*, 2514–2522.
58. Chen, W.; Zhang, S.; Tong, Q.; Zhang, X.; Zhao, H.; Ma, S.; Xiu, A.; He, Y. Regional Characteristics and Causes of Haze Events in Northeast China. *Chin. Geogr. Sci.* **2018**, *28*, 836–850. [CrossRef]
59. Zhao, R.; Gu, X.; Xue, B.; Zhang, J.; Ren, W. Short period PM 2.5 prediction based on multivariate linear regression model. *PLoS ONE* **2018**, *13*, e0201011. [CrossRef] [PubMed]
60. Yang, Y.; Ge, B.; Hao, S.; Xu, D.; Liu, Y.; Gan, L.; Wang, Z. Inversion of PM 2.5 concentration in Beijing based on visibility and AOD data. *Clim. Environ. Res.* **2020**, *25*, 521–530.
61. Song, Z.; Fu, D.; Zhang, X.; Han, X.; Song, J.; Zhang, J.; Wang, J.; Xia, X. MODIS AOD sampling rate and its effect on PM 2.5 estimation in North China. *Atmos. Environ.* **2019**, *209*, 14–22. [CrossRef]

62. Liu, S.; Bao, Y.; Jin, J.; Liu, C.; Xu, J.; Li, J.; Huang, J. Impact of aerosol radiative effect on surface ozone peaks during heavy haze events. *Plateau Meteorol.* **2018**, *37*, 296–304.
63. Jiao, L.; Xu, G.; Zhao, S.; Ma, M.; Dong, T.; Li, J. LUR-based Simulation of the Spatial Distribution of PM 2.5 of Wuhan. *Geomat. Inf. Sci. Wuhan. Univ.* **2015**, *40*, 1088–1094.
64. Liu, Y.; He, L.; Qin, W.; Lin, A.; Yang, Y. The effect of urban form on PM 2.5 concentration: Evidence from China's 340 prefecture-level cities. *Remote Sens.* **2021**, *14*, 7. [CrossRef]
65. Shi, T.; Hu, Y.; Liu, M.; Li, C.; Zhang, C.; Liu, C. Land use regression modelling of PM 2.5 spatial variations in different seasons in urban areas. *Sci. Total Environ.* **2020**, *743*, 140744. [CrossRef] [PubMed]
66. Li, J.; Gao, Y.; Huang, X. The impact of urban agglomeration on ozone precursor conditions: A systematic investigation across global agglomerations utilizing multi-source geospatial datasets. *Sci. Total Environ.* **2020**, *704*, 135458. [CrossRef] [PubMed]
67. Gao, L.; Tang, L.; Hou, H.; Wang, Y.; Mai, Y.; He, W.; Wang, W.; Su, H. The spatial-temporal distribution of air pollution and its relationship with landscape pattern in Shenzhen. *Acta Ecol. Sin.* **2021**, *41*, 8758–8770. [CrossRef]
68. Simon, H.; Fallmann, J.; Kropp, T.; Tost, H.; Bruse, M. Urban Trees and Their Impact on Local Ozone Concentration—A Microclimate Modeling Study. *Atmosphere* **2019**, *10*, 154. [CrossRef]
69. Huang, X.; Liu, Z.; Ge, Y.; Li, Q.; Wang, X.; Fu, H.; Zhu, J.; Zhou, B.; Wang, L.; George, C.; et al. Aerosol high water contents favor sulfate and secondary organic aerosol formation from fossil fuel combustion emissions. *npj Clim. Atmos. Sci.* **2023**, *6*, 173. [CrossRef]
70. Zhu, Y.; Bai, Y.; Xiong, J.; Zhao, T.; Xu, J.; Zhou, Y.; Meng, K.; Meng, C.; Sun, X.; Hu, W. Mitigation Effect of Dense "Water Network" on Heavy PM 2.5 Pollution: A Case Model of the Twain-Hu Basin, Central China. *Toxics* **2023**, *11*, 169. [CrossRef]
71. Zhu, D.; Zhou, X. Effect of urban water bodies on distribution characteristics of particulate matters and NO_2. *Sust. Cities Soc.* **2019**, *50*, 101679. [CrossRef]

Disclaimer/Publisher's Note: The statements, opinions and data contained in all publications are solely those of the individual author(s) and contributor(s) and not of MDPI and/or the editor(s). MDPI and/or the editor(s) disclaim responsibility for any injury to people or property resulting from any ideas, methods, instructions or products referred to in the content.